Research Article | Vol. 26, No. 20 | 1 Oct 2018 | OPTICS EXPRESS 26242
Optics EXPRESS

Efficient and broadband subwavelength grating coupler for 3.7 μm mid-infrared silicon photonics integration

NAN CHEN,[1,2] BOWEI DONG,[1,2] XIANSHU LUO,[3] HONG WANG,[4] NAVAB SINGH,[3] GUO-QIANG LO,[3] AND CHENGKUO LEE[1,2,*]

[1]*Department of Electrical and Computer Engineering, National University of Singapore, Singapore 117583, China*
[2]*Center for Intelligent Sensors and MEMS, National University of Singapore, 5 Engineering Drive 1, Singapore 117608, China*
[3]*NUS Suzhou Research Institute (NUSRI), Suzhou Industrial Park, Suzhou, 215123, China*
[4]*School of Electrical & Electronic Engineering, Nanyang Technological University, Singapore 639798, China*
*elelc@nus.edu.sg

Abstract: A grating coupler is an essential building block for compact and flexible photonics integration. In order to meet the increasing demand of mid-infrared (MIR) integrated photonics for sensitive chemical/gas sensing, we report a silicon-on-insulator (SOI) based MIR subwavelength grating coupler (SWGC) operating in the 3.7 μm wavelength range. We provide the design guidelines of a uniform and apodized SWGC, followed by numerical simulations for design verification. We experimentally demonstrate both types of SWGC. The apodized SWGC enables high coupling efficiency of –6.477 dB/facet with 3 dB bandwidth of 199 nm, whereas the uniform SWGC shows larger 3dB bandwidth of 263.5 nm but slightly lower coupling efficiency of −7.371 dB/facet.

1. Introduction

Mid-infrared region is abundant of vibrational fingerprints of chemical bonds of many kinds, which are attractive to molecular identification and detection [1]. Silicon photonics is one of the most promising platforms capable of sensitive spectroscopic sensing [2–4], in silicon photonics circuit configuration [5–7]. To make the photonics sensors compact even portable in the near future, efficiently converting the external light source (laser in most cases) into the in-plane waveguide is of much significance in terms of packaging flexibility, wafer level testing, etc. Therefore, grating coupler is becoming the preferable and main-steam choice [8].

There are several near- and mid-infrared grating couplers reported recently [9–19], others such as applied in the integrated evanescent field sensor [20], or in the integrated ring resonator system [21]. Figure 1 exhibits the collection to date of these reported works including simulation design. The simulation designs such as exploiting the SiGe coupler on the suspended waveguide at 4.5 μm [15], employing silicon-on-sapphire (SOS) with bottom reflector at 2.7 μm [14] and the Ge-on-Si3N4 platform with high index prism to suppress the dependence of diffracted angle on wavelength at 3.8 μm [16], theoretically open up more opportunities for efficient near- and mid-infrared grating couplers.

In 2012, N. Hattasan et al. proposed the shallow-etched SOI grating coupler with polysilicon overlay to accomplish the low coupling loss of −3.8 dB with 3 dB bandwidth of 90 nm at 2.1 μm [10]. Earlier in the same year, Z. Cheng et al. demonstrated the coupling efficiency of 32.6% for the transverse electric (TE) mode at 2.75 μm firstly through the shallow-etched subwavelength SOS grating coupler [11]. Around the same time, they also claimed the focusing suspended subwavelength grating coupler on SOI with the coupling efficiency of 24.7% at 2.75 μm [9]. Another similar work for 2 μm wavelength is presented

#328866 https://doi.org/10.1364/OE.26.026242
Journal © 2018 Received 7 May 2018; revised 1 Aug 2018; accepted 2 Aug 2018; published 24 Sep 2018

Optics EXPRESS

with the measured coupling efficiency of 24.3% in transverse magnetic (TM) mode [17]. When the focusing subwavelength grating is applied to the suspended membrane Ge waveguide, the coupling loss of –11 dB and 1 dB bandwidth of 58 nm has been experimentally proven for 2.37 μm [18]. Germanium with wide transparent window and high refractive index is drawing more attention to MIR photonics research. According to M. Nedeljkovic et al., the grating coupler established on the Ge-on-Si rib waveguide allows the transmission of –16.5 dB at 3.8 μm [13]. Further expanding the scope towards longer wavelength, the 5.2 μm shallow-etched grating coupler on Ge-on-Si enables the maximum efficiency of –5 dB and a 3 dB bandwidth of 100 nm, while the one on the Ge-on-SOI platform enables –4 dB and 180 nm [19]. The latest record is the Ge-on-Si grating coupler at 8.5 μm [22]. SOS is another alternative material catering to MIR grating coupler, i.e., the efficiency of 29% at 3.4 μm [12]. However, SOI platform has been well established and maturely developed for photonic integrated circuit over the past decades. Thus, we propose the fully SOI oriented MIR grating coupler for cost-effective and universal-adaptable purpose.

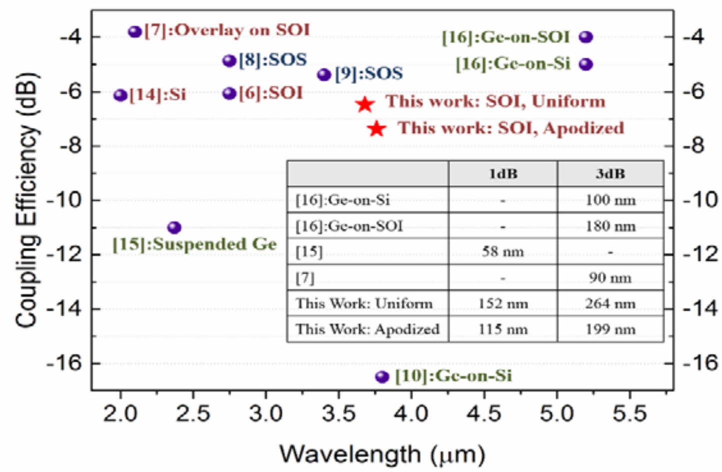

Fig. 1. Summary of the state-of-the-art demonstrations of the near- and mid-infrared grating couplers.

Since the year of 2009 when the subwavelength grating couplers were firstly materialized from conceptualization [23, 24], the subwavelength grating (SWG) is overwhelming owing to the higher degree of freedom for explicitly engineering the effective index contrast to alleviate the backside reflection, increase optical bandwidth, enhance the field overlap with fiber mode, etc [9, 18, 23–40]. After all, the three major factors adversely affecting the coupling efficiency are: poor directionality [40, 41], mode mismatch [42, 43] and back reflection [44]. Besides, the subwavelength grating can bypass the shallow etching which is difficult to control and requires extra processing steps. Moving towards MIR wavelength enlarges the SWG size accordingly, hence reducing the burden on complementary metal oxide semiconductor (CMOS) fabrication.

In the pursuit of the simplest structure and the easiest fabrication for the efficient grating couplers, SWGC is the desirable choice. Although some exotic techniques have been investigated for higher efficiency, such as the bottom metal mirror [39, 45, 46] and the multilayer Bragg reflector for the constructive interference [47], the overlay on the grating region to intrinsically diminish downward radiation [10, 48], the complexity of fabrication boosts up too. The additional bonding effort or the CMOS non-compatible process becomes the ultimate hurdle of the low-cost, mass production. Therefore, aiming for the low-cost yet efficient MIR fiber-to-chip coupling, we design and construct the SOI based SWGC for which only a single full etch with waveguide is required.

To the best of our knowledge, it is the first time that the SOI based subwavelength grating coupler at 3.7 μm is reported with the state-of-the-art coupling efficiency and optical bandwidth. In this paper, we start with introducing the SWGC design method, followed by presenting the simulated and measured results. Next, we show and analyze the difference between the uniform and the apodized grating couplers [34, 42]. Finally, we summarize the performances indexes of all the couplers and conclude with the best grating coupler designs for 3.7 μm.

2. Subwavelength grating coupler design

2.1 Fabrication method

Figure 2(a) illustrates the MIR subwavelength grating coupler, composed of waveguide output, taper and subwavelength grating. The devices were fabricated by the standard 8-inch CMOS process in IME, A*STAR. Starting from the commercially available SOI wafer with 220nm thick device layer and 3 μm thick buried oxide (BOX) layer, an additional 180nm thick device layer was epitaxially grown for mid-infrared application. So the ultimate thickness of BOX layer reached 400 nm. Followed by silicon oxide deposition as hard mask, the 193nm deep ultra-violet (DUV) photolithography was operated to define the high-quality pattern with the minimum linewidth of 200nm. Subsequently, the pattern was transferred to device layer by performing silicon reactive ion etching (RIE). The full etch of the SWG pattern reduces the complexity of fabrication. Then the wafer was coated with 3 μm thick silicon oxide and treated by chemical mechanical polishing (CMP), which ended up with a planarized 2 μm thick upper cladding layer. The output waveguide is 1.2-μm wide for the excellent confinement of the optical mode at 3.7 μm. The SWG's width (the production of number of unit cells N_y and periodicity P_y along y-axis) is matched with the core diameter of the single mode fiber at 10 μm; the length (the production of number of unit cells N_x and periodicity P_x along x-axis) is around 50 μm for uniform design and shorter for apodized design limited by the feature size in microfabrication. The end of SWGC is 5-μm long.

2.2 Design method

Applying Particle Swarm Optimization (PSO) [49] in the finite-difference time-domain (FDTD) simulation, taper length of 20 μm can be guaranteed with high transmission above 90% around 3.7 μm. The SWG pattern is uniform or apodized rectangle hole arranged in a periodic array as displayed in the inset. Figure 2(b) shows the schematic of fiber-coupler coupling where the actual oxide cladding is visually neglected. The single mode fiber is placed above the grating region at a tilted angle θ for encouraging mode match and suppressing the second-order Bragg back reflection loss. Scanning electron microscope (SEM) photo of Fig. 2(c) shows the apodized grating coupler of one facet. The couplers are in pairs connected back-to-back for measurement ease. Figure 2(d)-2(f) are the magnified SEM images of the SWG region of the unapodized, apodized in y-axis, apodized in x-axis designs, respectively.

Optics EXPRESS

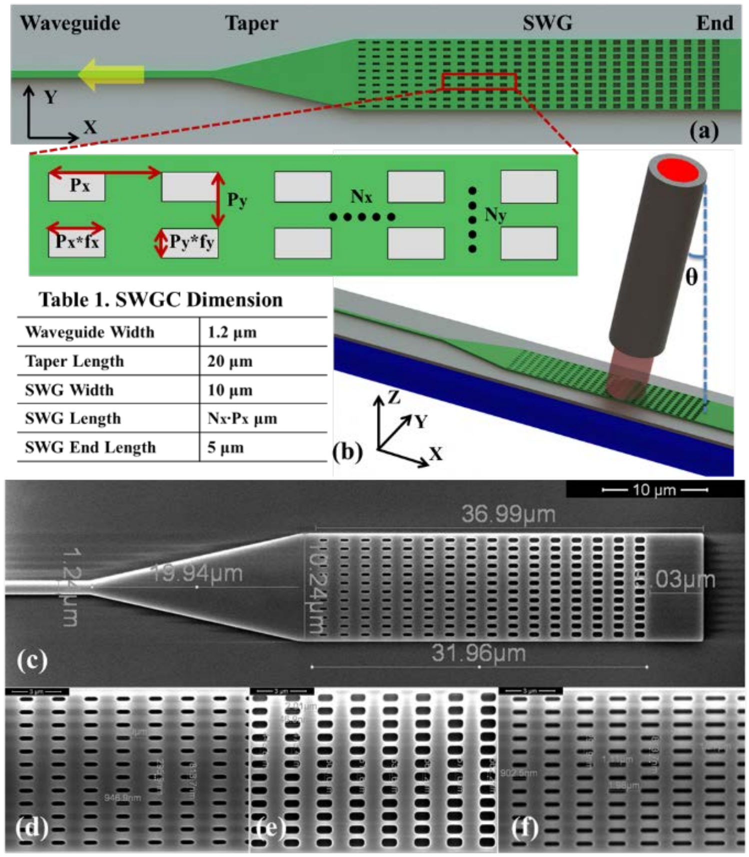

Table 1. SWGC Dimension

Waveguide Width	1.2 μm
Taper Length	20 μm
SWG Width	10 μm
SWG Length	Nx·Px μm
SWG End Length	5 μm

Fig. 2. (a) The top-viewed schematic of SWGC with inset of the zoomed-in SWG. (b) The schematic of grating coupler with input fiber placed at the angle of θ. (c) The SEM image of SWGC, device C2. (d) The SEM image of uniform SWG of device A1. (e) The SEM image of apodized SWG of device C2. (e) The SEM image of apodized SWG of device D1.

The design principle of grating coupler is based on the phase match condition (PMC) $n_{eff} = \lambda / P_x + n_c \sin\theta$ if only the first diffraction order is considered [31], where n_{eff} is the effective index of the grating region, θ is 13.5° in this work, n_c is the refractive index of cladding material which is silicon oxide and P_x is the grating periodicity along x-axis. The ultimate goal of design is to find the desired SWG dimensions: the periodicities of the subwavelength rectangle holes along x and y-axis, P_x and P_y; the filling factors of holes along x and y-axis, f_x and f_y, which are able to fulfill the requirement of PMC for the specific wavelength. However, there is no direct solution to these dimensions without being linked to the effective index n_{eff}. Therefore, the effective medium theory (EMT) that correlates the effective index with the dimensional parameters is deployed. Applying the zeroth-order TE mode EMT as shown in Eq. (1)-(2), and simultaneously assuming P_y is smaller than the Bragg periodicity to frustrate other disturbing diffractions, the two-dimensional subwavelength grating can be approximated to the one-dimensional grating model through projecting the y-axis periodic SWG component onto x-axis [23, 27, 40]:

Optics EXPRESS

$$n_{Lx} = \frac{1}{\sqrt{\frac{f_y}{n_{Ly}^2} + \frac{(1-f_y)}{n_{Hy}^2}}} \tag{1}$$

$$n_{eff} = f_x \cdot n_{Lx} + (1-f_x) \cdot n_{Hx}, \tag{2}$$

where n_{Ly} and n_{Hy} are the low and high refractive index in terms of the alternating subwavelength hole and silicon grating along y-axis, thus the values of which are 1.5 (for oxide cladding, 1 for air cladding) and 3.45, respectively. n_{Lx} is denoted as the low effective index of the one-dimensional region on x-axis, equivalently converted from the aforementioned alternating hole and silicon grating along y-axis by EMT method. n_{Hx} is the high effective index along x-axis, associated with the width w_{Hx} of the periodic silicon grating. In order to improve design accuracy (aiming the maximum coupling efficiency at 3.7 μm) n_{Hx} is simulated and fitted with respect to the silicon grating width before launching the numerical calculation. The correlation between n_{Hx} and w_{Hx} can be expressed as the cubic curve $n_{Hx} = 0.2 + 2.807 w_{Hx} - 1.192 w_{Hx}^2 + 0.173 w_{Hx}^3$, valid for uniform SWG with oxide cladding as shown in Fig. 3(a). Combining both n_{Lx} and n_{Hx} into EMT approximation, n_{eff} , the weighted average of the one-dimensional effective indexes along x-axis, would bridge the gap between the SWG unknown dimensions and PMC. When the n_{eff} values acquired from PMC and EMT are equal, SWG dimensions P_x , f_x , f_y can be finally confirmed, while P_y is chosen as 0.8 μm and 1 μm for comparison.

2.3 Optimization

Based on such design principle, more than one sets of dimension can meet the requirement. Verified by FDTD calculation, two designs are selected for possessing the optimum coupling efficiency of –4.3 dB (A1 and B1) at 3.7 μm, the wavelength of interest. To match with the single mode ZrF4 mid-infrared fiber in experiment setup, the fiber settings in the FDTD simulation are cladding diameter of 125 μm, cladding index of 1.47, and core diameter of 9 μm with index of 1.484.

Directionality for the fiber-to-chip coupling can be defined as the ratio of the transmitted optical power to the fraction of total diffracted optical power. The thickness of silicon device layer and BOX layer can strongly affect directionality due to the formation of constructive and destructive interference within the layers. In Fig. 3(b), device A1 with the silicon layer thicknesses ranging from 300 nm to 500 nm shows different characteristic of directionality when BOX layer is 3 μm thick. By extracting the directionality for each silicon thickness at 3.7 μm, the silicon thickness of 400nm is found to be able to achieve the optimum directionality of 53.05% as shown in Fig. 3(d). The dependence of directionality on the thickness of BOX layer is shown in Fig. 3(c) with 400 nm thick silicon layer. It can be observed that 3-μm thick BOX layer can provide high directionality.

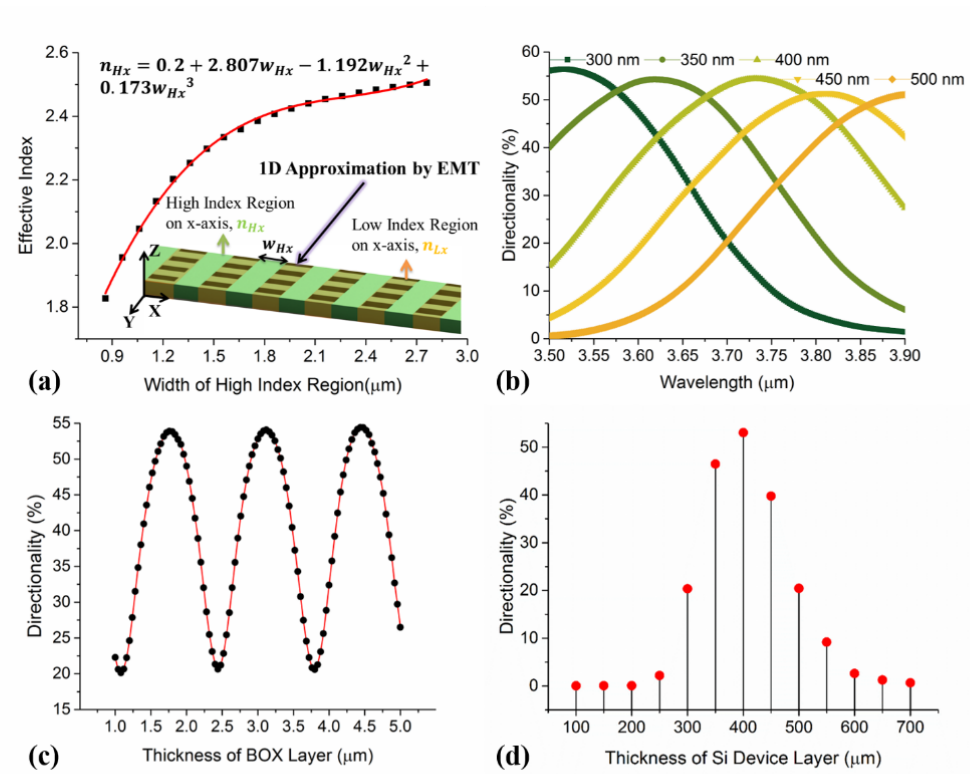

Fig. 3. (a) The correlation between the effective index and the width of the high index region by curve fitting. Inset: the schematic of 1D approximation EMT. (b) The simulated directionality of device A1 with different device layer thickness when the BOX layer is 3-μm thick from 3.5 μm to 3.9 μm. (c) The dependence of the simulated directionality on BOX layer thickness when the device layer is 400-nm thick for device A1. (d) The dependence of the simulated directionality on device layer thickness when the BOX layer is 3-μm thick for device A1.

The uniform designs are summarized in Table 1 with variations in x-axis periodicity. The y-axis periodicities for both group A and B are 0.8 μm, the filling factors along y-axis are 0.3 and the numbers of SWG repeated along x- and y-axis are 25 and 12. Starting from the prototype of uniform design A1, creating the chirped filling factor can be a satisfactory strategy to generate apodization along wave propagation direction. The apodized designs are thus different in terms of chirping form: group C with the apodized y-axis filling factor and group D with the apodized x-axis filling factor, which can refer to Table 2. The variation within group C is to alter the degree of apodization df_y , from weak to strong. Extra comparison for both apodized design groups is made between the y-axis periodicity of 0.8 μm and 1 μm.

Table 1. Design Summary of the Uniform SWGC

Device	P_x (μm)	f_x	N_x	P_y (μm)	f_y	N_y
A1	2	0.5	25	0.8	0.3	12
A2	1.95	0.5	25	0.8	0.3	12
A3	2.05	0.5	25	0.8	0.3	12
B1	2.05	0.58	25	0.8	0.3	12
B2	2	0.58	25	0.8	0.3	12
B3	2.1	0.58	25	0.8	0.3	12

Optics EXPRESS

Table 2. Design Summary of the Apodized SWGC

Device	P_x (μm)	$f_x = f_{x0} + df_x *n$	N_x	P_y (μm)	$f_y = f_{y0} + df_y *n$	N_y
C1	2	0.5	25	0.8	0.275 + 0.01n, n = 0, 1, 2,…, N_x	12
C2	2	0.5	24	0.8	0.275 + 0.02n, n = 0, 1, 2,…, N_x	12
C3	2	0.5	16	0.8	0.275 + 0.03n, n = 0, 1, 2,…, N_x	12
C4	2	0.5	24	1	0.275 + 0.02n, n = 0, 1, 2,…, N_x	12
D1	2	0.25 + 0.03n, n = 0, 1, 2,…, N_x	25	0.8	0.3	12
D2	2	0.25 + 0.03n, n = 0, 1, 2,…, N_x	25	1	0.3	12

3. Characterization and discussion

3.1 Characterization method

The measurement setup is shown in Fig. 4(a). Following the sequence of light path, the setup is consisted of a linearly polarized continuous wave tunable mid-infrared laser from Daylight Solution Inc (Model TLS-41038), chopper, half-wave plate, ZnSe lens (Thorlab), fiber connector to the input ZrF_4 mid-infrared fiber. Special fiber holder provides angle adjustment during measurement. Light travels through device chip on sample stage and couples to the output fiber. The light output will be received by mid-infrared detector (Horiba DSSIS020L) and processed by lock-in amplifier to reduce the noise level before reaching data processor. There are also top and rear microscopes around the sample holder to assist the alignment.

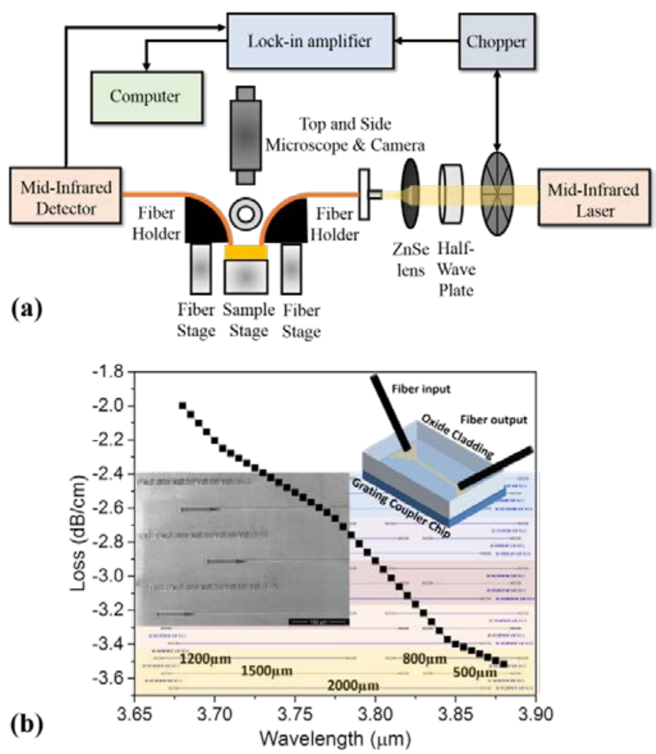

Fig. 4. (a) The mid-infrared optical photonics measurement setup for grating coupler. (b) The measured waveguide propagation loss spectrum. Insets: Layout of designs showing each grating coupler design with five different waveguide lengths, SEM photo and the schematic of fiber coupling.

The total loss η_{total} of the system from fiber input to fiber output contains the grating coupler loss from fiber-to-chip and chip-to-fiber coupling as well as waveguide loss $\eta_{waveguide}$. The waveguide loss can be obtained through multiplying the waveguide propagation loss by the length of waveguide. The measured waveguide propagation loss can be referred to in Fig. 4(b). We utilize the cutback technique to determine waveguide propagation loss by assigning five waveguides of different length to each coupler design: 500 µm, 800 µm, 1200 µm, 1500 µm and 2000 µm. The layout of design with the SEM photo is also provided in Fig. 4(b). Each color represents the same coupler design. For simplicity, it is assumed that the coupling losses of fiber-to-chip and chip-to-fiber are identical. Hence, the coupling efficiency η (or the aforementioned grating coupler loss) in dB can be calculated by $\eta = (\eta_{total} - \eta_{waveguide})/2$ in the characterization.

3.2 Result and discussion

FDTD simulation result is displayed as transmission spectrum, or coupling efficiency. The uniform designs are firstly calculated as in Fig. 5(a) and 5(c) that design A1 and B1 successfully produce transmission peak at 3.7 µm. Peak wavelength experiences red shift while P_x is lengthened which complies with Bragg condition. From Fig. 5 (b) and 5(d) it is worth noting that the measured spectra are exceedingly congruous with the simulated results in terms of peak shift, coupling efficiency change and spectrum profile, although the measured peak wavelength is slightly red-shifted by at most 50 nm and the measured coupling efficiency is decreased by 3 dB. In order to precisely attain 1 dB and 3 dB bandwidth, the measured spectra (in dB) are fit by parabola function resulted from the logarithm transformation from Gaussian profile in percentage, as described by the example of device A3 in Fig. 5(b). Generally, the measured bandwidth is narrower than the ideal case.

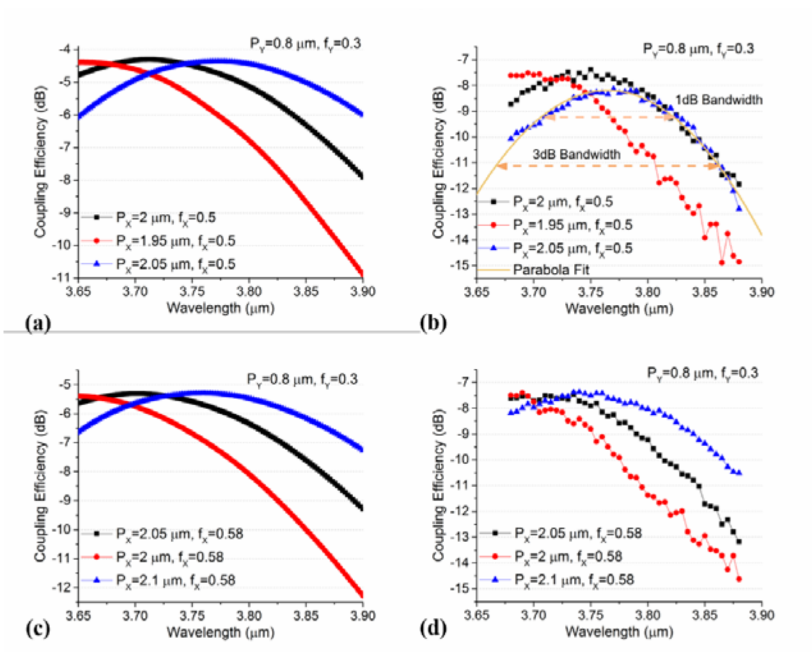

Fig. 5. (a) The simulated spectra of the uniform SWGC design A1, A2 and A3. (b) The measured spectra of the uniform SWGC device A1, A2 and A3 with an example of 3 dB and 1 dB bandwidth extraction of device A3 through parabola fit. (c) The simulated spectra of the uniform SWGC design B1, B2 and B3. (d) The measured spectra of the uniform SWGC device B1, B2 and B3.

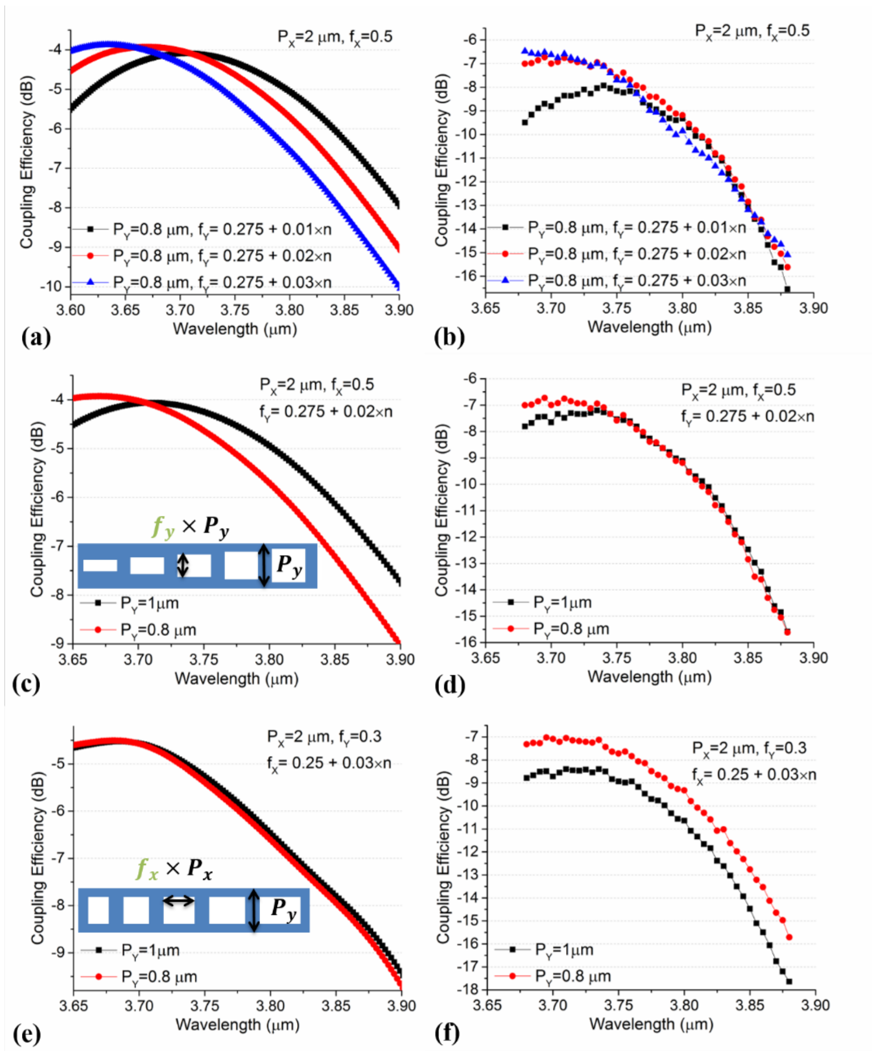

Fig. 6. (a) The simulated spectra of the apodized SWGC design C1, C2 and C3. (b) The measured spectra of the apodized SWGC device C1, C2 and C3. (c) The simulated spectra of the apodized SWGC design C2 and C4. Inset: the single row grating schematic showing the apodized f_y. (d) The measured spectra of the apodized SWGC device C2 and C4. (e) The simulated spectra of the apodized SWGC design D1 and D2. Inset: the single row grating schematic showing the apodized f_x. (f) The measured spectra of the apodized SWGC device D1 and D2.

Stemming from uniform design, the apodized couplers are engineered to remarkably circumvent the limitation of mode mismatch between fiber input and the coupled light. According to the simulation of apodized coupler, the maximum coupling efficiency can be enhanced by 0.5 dB but 3 dB bandwidth is reduced by 50 nm. Figure 6 shows the simulation and testing spectra of the apodized designs and devices. In Fig. 6(a) and 6(b), the increased df_y causes transmission peak blue-shifted and this is because that larger subwavelength hole size lowers effective index, causing the interference occurred at smaller wavelength. The measured spectra of device C1-C3 in Fig. 6(b) share the same pattern but with lower coupling efficiency and more significant wavelength shift and intensity drop.

Optics EXPRESS

Meanwhile, the impact of P_y is disclosed between C2 and C4, D1 and D2 in Fig. 6(c)-6(f) that smaller P_y could contribute higher peak coupling efficiency, verified by simulation and experiment. More specifically, for C2 and C4 apodized in f_y, the varying P_y leads to peak wavelength shift because the apodization of the effective index along y-axis will be partially modulated, thus the accumulated change drives wavelength shift. However, for D1 and D2 with the apodized f_x, the change of P_y does not impose much on the effective index along x-axis, hardly to cause noticeable wavelength shift.

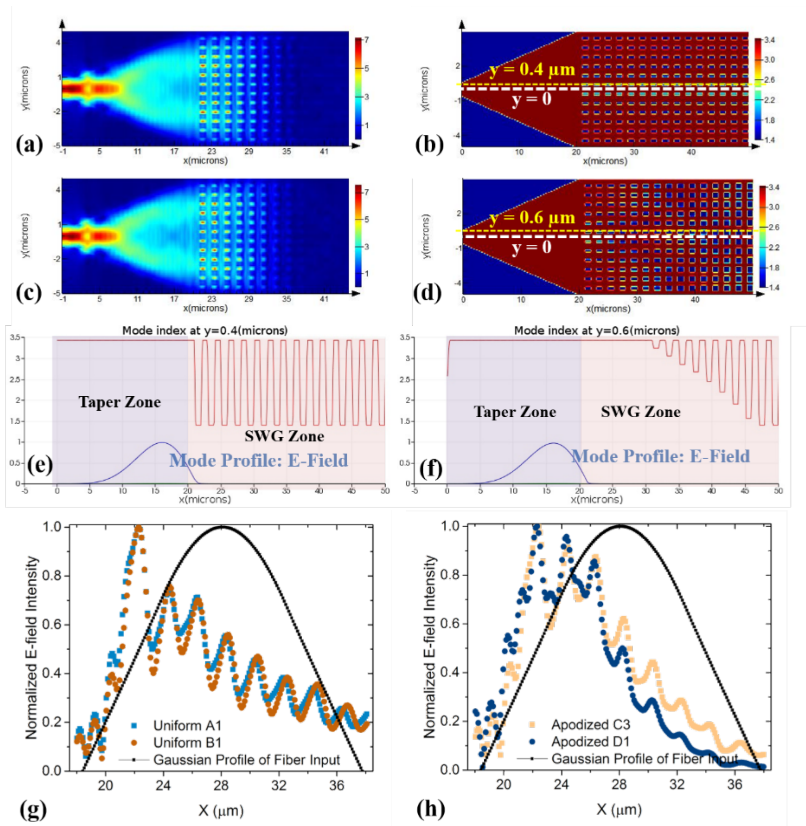

Fig. 7. (a) The simulated electric field distribution of design A1 (top view). (b) The simulated index of mode profile of design A1 (top view). (c) The simulated electric field distribution of design C3 (top view). (d) The simulated index of mode profile of design C3 (top view). (e) The simulated index of mode profile and electric field profile along x-axis in design A1. (f) The simulated index of mode profile and electric field profile along x-axis in design C3. (g) The diffracted modes from uniform coupler A1 and B1 versus the Gaussian profile of fiber input mode. (h) The diffracted modes from apodized coupler C3 and D1 versus the Gaussian profile of fiber input mode.

In order to gain the insightful knowledge of the difference between uniform and apodized gratings, the simulated electric field, index distribution of mode profile and the radiated grating mode of A1 and C3 at peak wavelengths are plotted in Fig. 7. From Fig. 7 (a) and 7(c), the electric field distribution mainly differs around taper center region and the very first SWGs close to taper. The distinguishing dissimilarities of the index distribution of mode profile are spotted within the SWG region in Fig. 7(b) and (d). Design A1 has a uniformly gradual index change with lower mode index at edge and higher index in the center. On the contrary, the mode index of C3 is arrow-like distributed along the light propagating direction.

Figure 7(e) and 7(f) portray the mode profile index of design A1 along y = 0.4 µm (to ensure probing swept across one entire row of subwavelength holes with fixed SWG hole width) and C3 along y = 0.6 µm (to ensure probing swept across one entire row of subwavelength holes with varied SWG hole width). The evenly alternating high-low mode profile index of uniform SWG zone ends up with weaker electric field of the waveguide mode than the gradually changing high-low index of apodized SWG zone. The mild and less intense index contrast modulated by the first few SWG holes next to the taper in the apodized SWGC structure is able to diminish the severe impedance discontinuity or suppress Fresnel reflection in the interface between the high and low index region [37]. In contrast, the sudden index change within the taper-uniform SWG transition region has difficulty in facilitating the initiate grating Bloch mode. Lastly, the diffracted beam modes of uniform and apodized grating are compared [23, 25], with the referenced Gaussian profile of fiber input in Fig. 7(g) and 7(h). It can be demonstrated by the normalized electric field profile that mode mismatch can be substantially mitigated via the approach of grating apodization. The apodized grating coupler can better assist and support mode overlap than the uniform grating coupler.

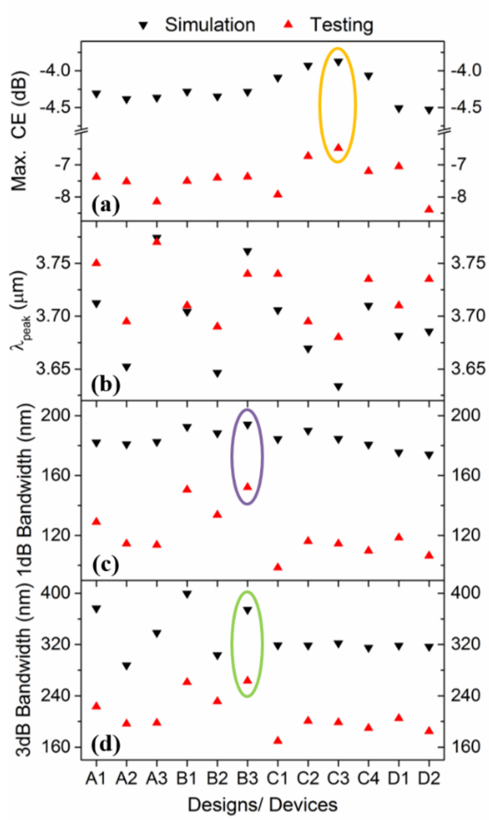

Fig. 8. (a) The simulated and measured maximum coupling efficiency of all design/devices with the marking of champion data. (b) The simulated and measured peak wavelength of all design/devices. (c) The simulated and measured 1 dB bandwidth of all design/devices with the marking of champion data. (d) The simulated and measured 3 dB bandwidth of all design/devices with the marking of champion data.

Here we have summarized the key parameters from measurement and simulation of the proposed couplers in Fig. 8: maximum coupling efficiency, peak wavelength, 1 dB and 3 dB bandwidth. The maximum simulated and measured coupling efficiencies are −3.872 dB and −6.477 respectively, contributed by the apodized design C3 [yellow circled in Fig. 8(a)]. The maximum coupling efficiency of the uniform grating design A and B, according to simulation

Optics EXPRESS

data, is lower than the apodized design C, and this has been consistently reproduced by experiment except for device C1 which is probably due to some random error in fabrication. In Fig. 8(b) of the simulated and measured peak wavelength comparison, the perceptible red shift is observed in the majority of the measured peak wavelengths, and this can be ascribed to alignment tolerance [47]. The measured peak wavelength changes in accordance with the dimension variation, validating the simulation results.

With respect to bandwidth, the simulated results outperform the measured ones. According to the previous research from Xia Chen *et al*., 1dB bandwidth can be determined by the effective index n_{eff} as Eq. (3) below [28, 30, 32, 3, 7, 44].

$$\Delta\lambda_{1dB} \propto \frac{n_c \cos\theta}{\left| \frac{n_{eff}(\lambda_p) - n_c \sin\theta}{\lambda_p} - \frac{dn_{eff}(\lambda)}{d\lambda} \right|} \tag{3}$$

where λ_p is the peak wavelength, i.e., 3.7 μm for the proposed design. This correlation reveals that low effective index would induce broad 1 dB/3 dB transmission band. Among the designs of A1, B1 and C1 aiming at 3.7 μm, the effective indexes of the uniform A1 (P_x = 2 μm) and B1 (P_x = 2.05 μm) are 2.188 and 2.143, and correspondingly, the simulated 1 dB bandwidths are 182 nm and 192 nm. The effective index of the apodized C1 is comparable to A1 so the simulated 1 dB bandwidth is 182nm. Since the measured peak wavelength is red-shifted, device A2, B2 and C2 instead have transmission peak at 3.7 μm and the measured 1 dB bandwidths are 114.5 nm, 133.7 nm and 116.1 nm, respectively.

The largest 1 dB and 3 dB bandwidths are offered by the uniform design B3 (and B1): 194 nm (simulated) and 152nm (measured) for 1 dB bandwidth, 374 nm (simulated, the maximum is 399.5nm by B1) and 263 nm (measured) for 3 dB bandwidth, respectively [purple circled in Fig. 8(c) and green circled in Fig. 8(d)]. Overall, the bandwidth of the apodized grating is found to be narrower than that of the unif orm grating. For instance, device C3 owns the maximum coupling efficiency at –6.477 dB, yet with 3 dB bandwidth of 198.6 nm; device B3 is equipped with the maximum 3 dB bandwidth of 263.5 nm but an average coupling efficiency at –7.371 dB. In order to assess grating coupler's performance in more comprehensive manner, we present a new Figure of merit *Area* taking both coupling efficiency and bandwidth into account.

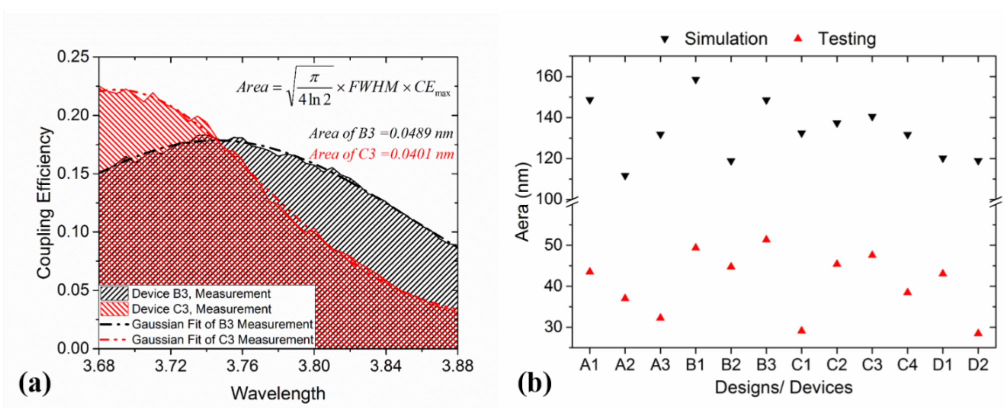

Fig. 9. (a) The measured coupling efficiency spectra of device B3 and C3 with the shaded area. The figure of merit *Area*'s calculation formula is inserted. The *Area* of device B3 is 0.0489 nm and 0.0401 nm, respectively. (b) The simulated and measured *Area* of all design/devices.

The area under the Gaussian profile of coupling efficiency is given as:

$$Area = \sqrt{\frac{\pi}{4\ln 2}} \times FWHM \times CE_{\max}, \tag{4}$$

in which FWHM is in the unit of nm and the maximum intensity of coupling efficiency is in unit one, thus the unit of the area is nm. Figure 9(a) displays the spectrum with the shaded area compared between device B3 and C3. Ignoring the cut-off wavelength range as a result of photo-detector's limited extremity, *Area* exhibits the overall transmission grating coupler offers over the entire wavelength range in reality. Figure 9(b) shows the different *Area* of all devices and device B3 beats the rest owing to its broad 3 dB bandwidth. Albeit device C3 has the champion coupling efficiency, lacking of large bandwidth makes it less competitive when it comes to the integral transmission.

4. Summary

We designed and demonstrated SOI based subwavelength grating couplers at 3.7 μm wavelength range. Starting from theoretical calculation, numerical simulation, and experimental demonstration, we thoroughly studied two different designs, respectively, the uniform and apodized SWGCs. While the apodized SWGCs showed higher coupling efficiency of −3.872 dB/facet by simulation, and −6.477 dB/facet experimentally, the uniform SWGC can provide larger bandwidth, with 1-dB and 3-dB bandwidth of respectively 152 nm and 263.5 nm. Such demonstrations are valuable building blocks for integrating out-of-plane light source with in-plane MIR silicon photonics system in the application of the high-quality sensing, light modulator and many more to explore in the spectral range of near- or mid-infrared.

Funding

National Research Foundation Singapore; Research Grant of CRP-15th (NRF-CRP001-019) "Piezoelectric Photonics Using CMOS Compatible AlN Technology for Enabling the Next Generation Photonics ICs and Nanosensors" at National University of Singapore, the NRF-ISF (NRF2015-NRF-ISF001-2620 NUS) "Reconfigurable data center optical interconnects using fast nanophotonic MEMS waveguide switches" and the partial support by National Natural Science Foundation of China under Grant No. 61474078 at NUS (Suzhou) Research Institute, Suzhou, China.

Acknowledgements

The authors would like to thank Xin Guo from SI-COE lab, OPTIMUS, Photonics Center of Excellence of Nanyang Technological University for the great support on her guidance of setup and measurement.

References

1. P. T. Lin, V. Singh, J. Hu, K. Richardson, J. D. Musgraves, I. Luzinov, J. Hensley, L. C. Kimerling, and A. Agarwal, "Chip-scale Mid-Infrared chemical sensors using air-clad pedestal silicon waveguides," Lab Chip **13**(11), 2161–2166 (2013).
2. M. C. Estevez, M. Alvarez, and L. M. Lechuga, "Integrated optical devices for lab-on-a-chip biosensing applications," Laser Photonics Rev. **6**(4), 463–487 (2012).
3. M. Sieger and B. Mizaikoff, "Toward On-Chip Mid-Infrared Sensors," Anal. Chem. **88**(11), 5562–5573 (2016).
4. B. Dong, X. Guo, C. P. Ho, B. Li, H. Wang, C. Lee, X. Luo, and G. Q. Lo, "Silicon-on-Insulator Waveguide Devices for Broadband Mid-Infrared Photonics," IEEE Photonics J. **9**, 1–10 (2017).
5. B. Dong, X. Luo, T. Hu, T. X. Guo, H. Wang, D. L. Kwong, P. G. Q. Lo, and C. Lee, "Compact Low Loss Mid-Infrared Wavelength-Flattened Directional Coupler (WFDC) for Arbitrary Power Splitting Ratio Enabled by Rib Waveguide Dispersion Engineering," IEEE J. Sel. Top. Quantum Electron. **24**(4), 1–8 (2018).
6. Y. Ma, B. Dong, B. Li, J. Wei, Y. Chang, C. P. Ho, and C. Lee, "Mid-Infrared Slow Light Engineering and Tuning in 1-D Grating Waveguide," IEEE J. Sel. Top. Quantum Electron. **24**, 1–8 (2018).
7. G. Roelkens, U. Dave, A. Gassenq, N. Hattasan, C. Hu, B. Kuyken, F. Leo, A. Malik, M. Muneeb, E. Ryckeboer, S. Uvin, Z. Hens, R. Baets, Y. Shimura, F. Gencarelli, B. Vincent, R. Loo, J. Van Campenhout, L. Cerutti, J.-B. Rodriguez, E. Tournié, X. Chen, M. Nedeljkovic, G. Mashanovich, L. Shen, N. Healy, A. C.

Peacock, X. Liu, R. Osgood, and W. Green, "Silicon-based heterogeneous photonic integrated circuits for the mid-infrared," Opt. Mater. Express **3**(9), 1523–1536 (2013).
8. L. Zhu, W. Yang, and C. Chang-Hasnain, "Very high efficiency optical coupler for silicon nanophotonic waveguide and single mode optical fiber," Opt. Express **25**(15), 18462–18473 (2017).
9. Z. Cheng, X. Chen, C. Y. Wong, K. Xu, C. K. Y. Fung, Y. M. Chen, and H. K. Tsang, "Focusing subwavelength grating coupler for mid-infrared suspended membrane waveguide," Opt. Lett. **37**(7), 1217–1219 (2012).
10. N. Hattasan, B. Kuyken, F. Leo, E. M. P. Ryckeboer, D. Vermeulen, and G. Roelkens, "High-Efficiency SOI Fiber-to-Chip Grating Couplers and Low-Loss Waveguides for the Short-Wave Infrared," IEEE Photon. Technol. Lett. **24**(17), 1536–1538 (2012).
11. C. Zhenzhou, C. Xia, C. Y. Wong, X. Ke, C. K. Y. Fung, Y. M. Chen, and T. Hon Ki, "Mid-Infrared Grating Couplers for Silicon-on-Sapphire Waveguides," IEEE Photon. J. **4**, 104–113 (2012).
12. Y. Zou, H. Subbaraman, S. Chakravarty, X. Xu, A. Hosseini, W. C. Lai, P. Wray, and R. T. Chen, "Grating-coupled silicon-on-sapphire integrated slot waveguides operating at mid-infrared wavelengths," Opt. Lett. **39**(10), 3070–3073 (2014).
13. M. Nedeljkovic, J. S. Penades, C. J. Mitchell, A. Z. Khokhar, S. Stankovic, T. D. Bucio, C. G. Littlejohns, F. Y. Gardes, and G. Z. Mashanovich, "Surface-Grating-Coupled Low-Loss Ge-on-Si Rib Waveguides and Multimode Interferometers," IEEE Photon. Technol. Lett. **27**(10), 1040–1043 (2015).
14. J. Zhang, J. Yang, W. Wu, H. Jia, and S. Chang, "High performance silicon-on-sapphire subwavelength grating coupler for 2.7μm wavelength," in *2015 International Conference on Photonics, Optics and Laser Technology (PHOTOPTICS)*, 2015), 67–72.
15. H. Schröder, R. T. Chen, J. Favreau, C. Durantin, J.-M. Fédéli, S. Boutami, and G.-H. Duan, "Suspended mid-infrared fiber-to-chip grating couplers for SiGe waveguides," Proc. SPIE **9753**, 975319 (2016).
16. P. Cheben, J. Čtyroký, I. Molina-Fernández, A. Sánchez-Postigo, J. G. Wangüemert-Pérez, J. M. Luque-González, Í. Molina-Fernández, P. Cheben, C. A. Alonso-Ramos, R. Halir, J. H. Schmid, and A. Ortega-Moñux, "Broadband high-efficiency zero-order surface grating coupler for the near- and mid-infrared wavelength ranges," Proc. SPIE **10242**, 102420E (2017).
17. J. Li, L. Liu, W. Sun, X. Wen, K. Xu, and Q. Song, "The 2-μm fully-etched silicon grating coupler," in *2017 Conference on Lasers and Electro-Optics Pacific Rim (CLEO-PR)*, 1–3 (2017).
18. J. Kang, Z. Cheng, W. Zhou, T.-H. Xiao, K.-L. Gopalakrisna, M. Takenaka, H. K. Tsang, and K. Goda, "Focusing subwavelength grating coupler for mid-infrared suspended membrane germanium waveguides," Opt. Lett. **42**(11), 2094–2097 (2017).
19. S. Radosavljevic, B. Kuyken, and G. Roelkens, "Efficient 5.2 μm wavelength fiber-to-chip grating couplers for the Ge-on-Si and Ge-on-SOI mid-infrared waveguide platform," Opt. Express **25**(16), 19034–19042 (2017).
20. J. Kasberger, A. Saeed, T. Fromherz, S. Katletz, and B. Jakoby, "Spectral Resolution of the Grating Coupler of a Miniaturized Integrated Evanescent Field IR Absorption Sensor," IEEE J. Quantum Electron. **47**(7), 950–958 (2011).
21. R. Shankar, I. Bulu, and M. Lončar, "Integrated high-quality factor silicon-on-sapphire ring resonators for the mid-infrared," Appl. Phys. Lett. **102**(5), 051108 (2013).
22. M. Nedeljkovic, J. S. Penades, V. Mittal, G. S. Murugan, A. Z. Khokhar, C. Littlejohns, L. G. Carpenter, C. B. E. Gawith, J. S. Wilkinson, and G. Z. Mashanovich, "Germanium-on-silicon waveguides operating at mid-infrared wavelengths up to 8.5 μm," Opt. Express **25**(22), 27431–27441 (2017).
23. R. Halir, P. Cheben, S. Janz, D.-X. Xu, I. Molina-Fernández, and J. G. Wangüemert-Pérez, "Waveguide grating coupler with subwavelength microstructures," Opt. Lett. **34**(9), 1408–1410 (2009).
24. C. Xia and H. K. Tsang, "Nanoholes Grating Couplers for Coupling Between Silicon-on-Insulator Waveguides and Optical Fibers," IEEE Photonics J. **1**(3), 184–190 (2009).
25. R. Halir, P. Cheben, J. H. Schmid, R. Ma, D. Bedard, S. Janz, D. X. Xu, A. Densmore, J. Lapointe, and I. Molina-Fernández, "Continuously apodized fiber-to-chip surface grating coupler with refractive index engineered subwavelength structure," Opt. Lett. **35**(19), 3243–3245 (2010).
26. K. Yvind and J. M. Hvam, "High-efficiency, large-bandwidth silicon-on-insulator grating coupler based on a fully-etched photonic crystal structure," Appl. Phys. Lett. **96**(5), 051126 (2010).
27. X. Chen and H. K. Tsang, "Polarization-independent grating couplers for silicon-on-insulator nanophotonic waveguides," Opt. Lett. **36**(6), 796–798 (2011).
28. X. Chen, K. Xu, Z. Cheng, C. K. Y. Fung, and H. K. Tsang, "Wideband subwavelength gratings for coupling between silicon-on-insulator waveguides and optical fibers," Opt. Lett. **37**(17), 3483–3485 (2012).
29. Z. Cheng, X. Chen, C. Y. Wong, K. Xu, and H. K. Tsang, "Mid-infrared Suspended Membrane Waveguide and Ring Resonator on Silicon-on-Insulator," IEEE Photon. J. **4**(5), 1510–1519 (2012).
30. Z. Cheng, X. Chen, C. Y. Wong, K. Xu, and H. K. Tsang, "Broadband focusing grating couplers for suspended-membrane waveguides," Opt. Lett. **37**(24), 5181–5183 (2012).
31. J. Kubby, X. Chen, Z. Cheng, C. K. Y. Fung, H. K. Tsang, and G. T. Reed, "Design and applications of silicon waveguide grating couplers," Proc. SPIE **8266**, 82660I (2012).
32. X. Xu, H. Subbaraman, J. Covey, D. Kwong, A. Hosseini, and R. T. Chen, "Colorless grating couplers realized by interleaving dispersion engineered subwavelength structures," Opt. Lett. **38**(18), 3588–3591 (2013).
33. C. Alonso-Ramos, P. Cheben, A. Ortega-Moñux, J. H. Schmid, D. X. Xu, and I. Molina-Fernández, "Fiber-chip grating coupler based on interleaved trenches with directionality exceeding 95," Opt. Lett. **39**(18), 5351–5354 (2014).

Optics EXPRESS

34. D. Benedikovic, P. Cheben, J. H. Schmid, D.-X. Xu, J. Lapointe, S. Wang, R. Halir, A. Ortega-Moñux, S. Janz, and M. Dado, "High-efficiency single etch step apodized surface grating coupler using subwavelength structure," Laser Photonics Rev. **8**(6), L93–L97 (2014).
35. Z. Cheng and H. K. Tsang, "Experimental demonstration of polarization-insensitive air-cladding grating couplers for silicon-on-insulator waveguides," Opt. Lett. **39**(7), 2206–2209 (2014).
36. Y. Ding, C. Peucheret, H. Ou, and K. Yvind, "Fully etched apodized grating coupler on the SOI platform with -0.58 dB coupling efficiency," Opt. Lett. **39**(18), 5348–5350 (2014).
37. Q. Zhong, V. Veerasubramanian, Y. Wang, W. Shi, D. Patel, S. Ghosh, A. Samani, L. Chrostowski, R. Bojko, and D. V. Plant, "Focusing-curved subwavelength grating couplers for ultra-broadband silicon photonics optical interfaces," Opt. Express **22**(15), 18224–18231 (2014).
38. D. Benedikovic, C. Alonso-Ramos, P. Cheben, J. H. Schmid, S. Wang, D. X. Xu, J. Lapointe, S. Janz, R. Halir, A. Ortega-Moñux, J. G. Wangüemert-Pérez, I. Molina-Fernández, J. M. Fédéli, L. Vivien, and M. Dado, "High-directionality fiber-chip grating coupler with interleaved trenches and subwavelength index-matching structure," Opt. Lett. **40**(18), 4190–4193 (2015).
39. D. Benedikovic, P. Cheben, J. H. Schmid, D. X. Xu, B. Lamontagne, S. Wang, J. Lapointe, R. Halir, A. Ortega-Moñux, S. Janz, and M. Dado, "Subwavelength index engineered surface grating coupler with sub-decibel efficiency for 220-nm silicon-on-insulator waveguides," Opt. Express **23**(17), 22628–22635 (2015).
40. D. Benedikovic, C. Alonso-Ramos, P. Cheben, J. H. Schmid, S. Wang, R. Halir, A. Ortega-Moñux, D. X. Xu, L. Vivien, J. Lapointe, S. Janz, and M. Dado, "Single-etch subwavelength engineered fiber-chip grating couplers for 1.3 µm datacom wavelength band," Opt. Express **24**(12), 12893–12904 (2016).
41. C. Li, H. Zhang, M. Yu, and G. Q. Lo, "CMOS-compatible high efficiency double-etched apodized waveguide grating coupler," Opt. Express **21**(7), 7868–7874 (2013).
42. X. Chen, C. Li, C. K. Y. Fung, S. M. G. Lo, and H. K. Tsang, "Apodized Waveguide Grating Couplers for Efficient Coupling to Optical Fibers," IEEE Photon. Technol. Lett. **22**(15), 1156–1158 (2010).
43. M. Antelius, K. B. Gylfason, and H. Sohlström, "An apodized SOI waveguide-to-fiber surface grating coupler for single lithography silicon photonics," Opt. Express **19**(4), 3592–3598 (2011).
44. Y. Wang, X. Wang, J. Flueckiger, H. Yun, W. Shi, R. Bojko, N. A. F. Jaeger, and L. Chrostowski, "Focusing sub-wavelength grating couplers with low back reflections for rapid prototyping of silicon photonic circuits," Opt. Express **22**(17), 20652–20662 (2014).
45. W. S. Zaoui, A. Kunze, W. Vogel, M. Berroth, J. Butschke, F. Letzkus, and J. Burghartz, "Bridging the gap between optical fibers and silicon photonic integrated circuits," Opt. Express **22**(2), 1277–1286 (2014).
46. Y. Ding, C. Peucheret, H. Ou, and K. Yvind, "Fully etched apodized grating coupler on the SOI platform with -0.58 dB coupling efficiency," Opt. Lett. **39**(18), 5348–5350 (2014).
47. T. Dirk, L. Frederik Van, A. Melanie, B. Wim, T. Dries Van, B. Peter, and B. Roel, "Grating Couplers for Coupling between Optical Fibers and Nanophotonic Waveguides," Jpn. J. Appl. Phys. **45**, 6071–6077 (2006).
48. D. Vermeulen, S. Selvaraja, P. Verheyen, G. Lepage, W. Bogaerts, P. Absil, D. Van Thourhout, and G. Roelkens, "High-efficiency fiber-to-chip grating couplers realized using an advanced CMOS-compatible silicon-on-insulator platform," Opt. Express **18**(17), 18278–18283 (2010).
49. "https://kb.lumerical.com/en/sweeps_optimization.html.